

Tunable geometric photocurrent in van der Waals heterostructure: supplement

**ABDULLAH RASMITA,^{1,†}  CHONGYUN JIANG,^{1,2,6,†}  HUI MA,^{1,3}
ZHURUN JI,⁴  RITESH AGARWAL,⁴ AND WEI-BO GAO^{1,5,7} **

¹*Division of Physics and Applied Physics, School of Physical and Mathematical Sciences, Nanyang Technological University, Singapore 637371, Singapore*

²*College of Electronic Information and Optical Engineering, Nankai University, Tianjin 300350, China*

³*School of Physical Science and Technology, Tiangong University, Tianjin 300387, China*

⁴*Department of Materials Science and Engineering, University of Pennsylvania, Philadelphia, Pennsylvania 19104, USA*

⁵*The Photonics Institute and Centre for Disruptive Photonic Technologies, Nanyang Technological University, Singapore 637371, Singapore*

⁶*e-mail: jiang.chongyun@nankai.edu.cn*

⁷*e-mail: wbgao@ntu.edu.sg*

[†]*These authors contributed equally to this work.*

This supplement published with The Optical Society on 8 September 2020 by The Authors under the terms of the [Creative Commons Attribution 4.0 License](https://creativecommons.org/licenses/by/4.0/) in the format provided by the authors and unedited. Further distribution of this work must maintain attribution to the author(s) and the published article's title, journal citation, and DOI.

Supplement DOI: <https://doi.org/10.6084/m9.figshare.12746201>

Parent Article DOI: <https://doi.org/10.1364/OPTICA.393381>

Tunable geometric photocurrent in van der Waals heterostructure: supplementary material

ABDULLAH RASMITA,^{1,†} CHONGYUN JIANG,^{1,2,*†} HUI MA,^{1,3} ZHURUN JI,⁴ RITESH AGARWAL,⁴ AND WEI-BO GAO^{1,5,*}

¹Division of Physics and Applied Physics, School of Physical and Mathematical Sciences, Nanyang Technological University, Singapore 637371, Singapore

²College of Electronic Information and Optical Engineering, Nankai University, Tianjin 300350, China

³School of Physical Science and Technology, Tiangong University, Tianjin 300387, China

⁴Department of Materials Science and Engineering, University of Pennsylvania, Philadelphia, PA 19104, USA

⁵The Photonics Institute and Centre for Disruptive Photonic Technologies, Nanyang Technological University, 637371 Singapore, Singapore

[†]These authors contributed equally to this work.

*Corresponding author: jiang.chongyun@nankai.edu.cn, wbgao@ntu.edu.sg

Published XX Month XXXX

This document provides supplementary information to "Tunable geometric photocurrent in van der Waals heterostructure". Note 1 describes the excitation power and wavelength dependence of the circular photocurrent. Note 2 describes the circular photocurrent map taken on another sample. Note 3 describes the circular photocurrent map for various electrode configurations. Note 4 and Note 5 describe additional discussions on the source-drain and the back gate voltage dependence of the circular photocurrent, respectively.

Note 1: Excitation power and wavelength dependence of the circular photocurrent

The power and wavelength dependence of I_{CPGE} at temperature 140 K is shown in Fig. S1(a) and S1(b), respectively. Regarding the power dependence, I_{CPGE} shows a linear relationship with the excitation power. This is because it grows linearly with the population of the photo-induced carrier, which in turn depends linearly on the excitation power.

Regarding the wavelength dependence, I_{CPGE} reaches a maximum magnitude at the excitation wavelength ~ 720 nm (i.e., the charged WSe₂ exciton peak[1]). The sharp decrease of the I_{CPGE} magnitude for excitations above 720 nm is because excitations with these wavelengths do not have enough energy to excite the intralayer exciton. As a result, there is no photo-induced carrier generated. The decrease in the I_{CPGE} magnitude for excitations below 720 nm can be understood by considering that an off-resonant excitation results in a higher intervalley scattering rate of the intralayer exciton[2]. This results in a weaker correspondence between the circular polarization and the carrier valley polarization, which causes the reduction of the I_{CPGE} magnitude.

Note 2: Circular photocurrent map on another MoS₂/WSe₂ heterostructure sample

To check the reproducibility of the result, we fabricated another MoS₂/WSe₂ device and took the circular photocurrent map under a zero source-drain bias. For this sample, we found that the circular photocurrent map is more apparent when we apply a 5V gate voltage. The optical image of the sample and the circular photocurrent map for one electrode pair configuration is shown in Fig. S2(a) and (b), respectively. From these figures, we can see that, qualitatively, the conclusion that we obtained from the other device is still applicable. In particular, it can be seen that the two orthogonal sides of the same current-collecting electrode have opposite circular photocurrent polarity, while the parallel sides have the same circular photocurrent polarity.

Note 3: Circular photocurrent map for various electrode pair configurations

The circular photocurrent maps at room temperature for various electrode pair configurations are shown in Fig. S3(a-i), while the maps at low temperature (140 K) are shown in Fig. S4(a-i). As can be seen from these figures, the observation that the I_{CPGE} magnitude becomes larger as the excitation gets closer to the edge of an electrode is valid

regardless of the electrode pair configuration. Also, the I_{CPGE} magnitude at 140 K is larger than that at 295 K. This can be attributed to higher carrier mobility (longer relaxation time) at a lower temperature.

Note 4: More discussion on the source-drain voltage dependence of the circular photocurrent

From Fig. 2(d) in the main text, it can be seen that I_{CPGE} seems to be saturating for $V_{SD} > 0.05$ V, while it is not saturating for $V_{SD} < -0.05$ V.

The seemingly asymmetric saturation behavior may be related to the reduction of the relaxation time as the value of V_{SD} is increased. When the source-drain voltage V_{SD} is applied, the back gate is grounded. Hence, increasing V_{SD} has a similar electrical doping effect with decreasing V_G . As has been shown in Fig. 3(a) in the main text, the magnitude of I_{CPGE} decreases with decreasing V_G (increasing V_{SD}), which we attributed to the reduction of the relaxation time. Moreover, looking at the green and blue data points in Fig. 3(a), we can see that this reduction only starts to happen at some value of V_G .

Taking all of these into consideration, we can imagine a scenario where the relaxation time is roughly constant as V_{SD} is increased from -0.15 V to 0.05 V and it starts to decrease as V_{SD} is increased to more than 0.05 V. As a result, the circular photocurrent shows a saturation behavior for $V_{SD} > 0.05$ V. This effect, together with the higher-order nonlinear effects such as nonlinear valley current [3] and the electric field-induced circular dichroism modulation [4], may need to be taken into account for large V_{SD} cases.

Note 5: More discussion on the back gate voltage dependence of the circular photocurrent

There are four mechanisms where the back gate voltage can affect the circular photocurrent:

1. It can induce an out-of-plane electric field inside the heterostructure which can affect the exciton dissociation when the energy shift due to the electric field is in the same order as the TMD material band gap [5, 6].
2. It can change the Fermi level of each layer through the electrical doping which results in a change in the built-in electric field.
3. Because the top electrodes are smaller than both the sample and the bottom electrode, an in-plane electric field in the heterostructure can be generated by the back gating.
4. The back gate-induced electrical doping changes the carrier mobility and the relaxation time in the heterostructure (as discussed in the manuscript).

To analyze the first and second mechanisms, we can use the capacitance-in-series model (Fig. S5). Similar to Ref. [7], in our case, the top electrode is in contact with both layers: WSe₂ (inside the heterostructure region) and MoS₂ (outside the heterostructure region). We use the approximation

$$C_q^W = C_q^M \approx \frac{m_0 e^2}{\pi \hbar^2}$$

for the quantum capacitance, which is the case when the Fermi level is close to the band edge [7]. From this model the Fermi level shift in WSe₂ (Δ_W) and MoS₂ (Δ_M), as well as the out-of-plane electric field (E_{OP}^G , direction: from MoS₂ to WSe₂) in the heterostructure below the electrode can be estimated as $\Delta_W \approx 14.6V_G$, $\Delta_M \approx 185.3V_G$, and $E_{OP}^G \approx 7 \times 10^{-6} V_G$ where the energy, voltage, and electric field is in μeV , V, and MV/cm, respectively. Given that the highest V_G in our experiment is around 20 V, the maximum value for each parameter is $\Delta_W \approx 0.3$ meV, $\Delta_M \approx 3.7$ meV, and $E_{OP}^G \approx 1.4 \times 10^{-4}$ MV/cm, respectively. Both energy shifts are more than two orders of magnitude smaller than the built-in barrier height (~ 0.9 eV for WSe₂/Au contact) and the material band gap. Hence, the first and second mechanisms can be neglected.

The in-plane electric field caused by the third mechanism can be obtained from the electric field distribution simulation. The result is shown in Fig. S6(a, b). We note here that the in-plane conductivity of the heterostructure layer (measured value ~ 0.01 μS) must be considered in the simulation to obtain a realistic result. We have also included the simulation result for the source-drain bias case (Fig. S6(c, d)). As can be seen from the simulation result, the in-plane electric field due to the third mechanism is $E_{IP}^G \approx 2 \times 10^{-8} V_G$, while the in-plane electric field due to source drain bias V_{SD} is $E_{IP}^{SD} \approx 0.01 V_{SD}$ (electric field in MV/cm and voltage in V).

Given that the highest V_G in our experiment is around 20 V while the highest V_{SD} is around 0.15 V, the maximum value for each in-plane electric fields are $E_{IP}^G \approx 4 \times 10^{-7}$ MV/cm and $E_{IP}^{SD} \approx 1.5 \times 10^{-3}$ MV/cm. As can be seen from these values, in our experiment, the V_{SD} -induced electric field ($E_{IP}^{SD} \approx 1.5 \times 10^{-3}$ MV/cm) is more than one order magnitude bigger than the V_G -induced electric field ($E_{IP}^G \approx 4 \times 10^{-7}$ MV/cm and $E_{OP}^G \approx 1.4 \times 10^{-4}$ MV/cm). Hence, we can conclude that only the fourth mechanism is effective in modulating the circular photocurrent.

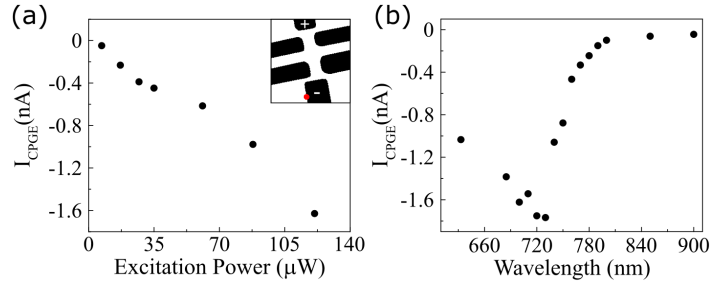


Fig. S1. Power and wavelength dependence of the circular photocurrent at a low temperature (140K). (a) Circular photocurrent as a function of the excitation power. The excitation wavelength used here is 720 nm. The inset shows the excitation location and the electrode configuration. (b) Circular photocurrent as a function of the excitation wavelength. The excitation power is maintained around 140 to 155 μW . The excitation location and the electrode configuration are the same as in Fig. S1(a).

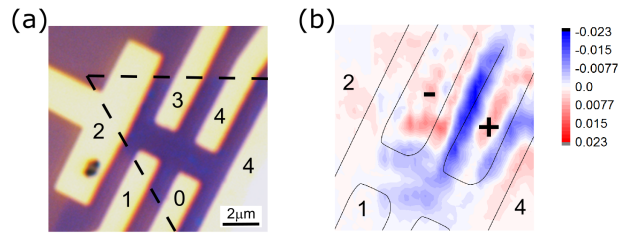


Fig. S2. Circular photocurrent map at room temperature for another $\text{MoS}_2/\text{WSe}_2$ heterostructure device. (a) The layout of the device. The two electrodes numbered 4 are shorted to each other. The dashed line shows the boundary of the heterostructure. (b) Circular photocurrent map with source: electrode 3 and drain: electrode 4. There is no source-drain bias applied to the sample. The gate voltage of 5V is used. The unit of the circular photocurrent is nA.

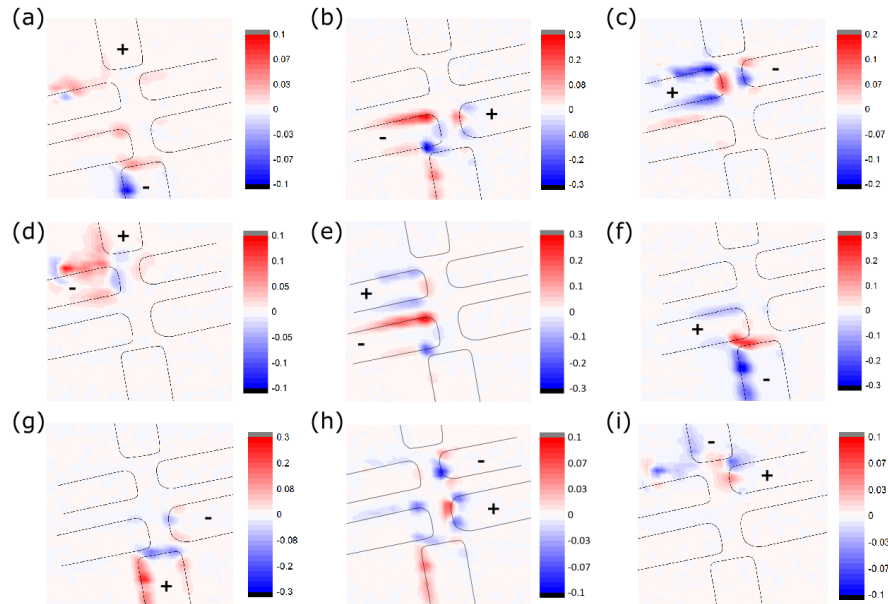


Fig. S3. Circular photocurrent map at room temperature (295 K) for various electrode pair configurations. All of these data are obtained using 720 nm 115 μW optical excitations. The unit of the circular photocurrent is nA. In all cases, the circular photocurrent is much more apparent when the excitation is near the electrode edge compared to other excitation locations. The (+)/(-) indicates the current-collecting electrode, i.e., the current is positive if it flows from the (+) electrode to the (-) electrode. The source-drain bias is not applied.

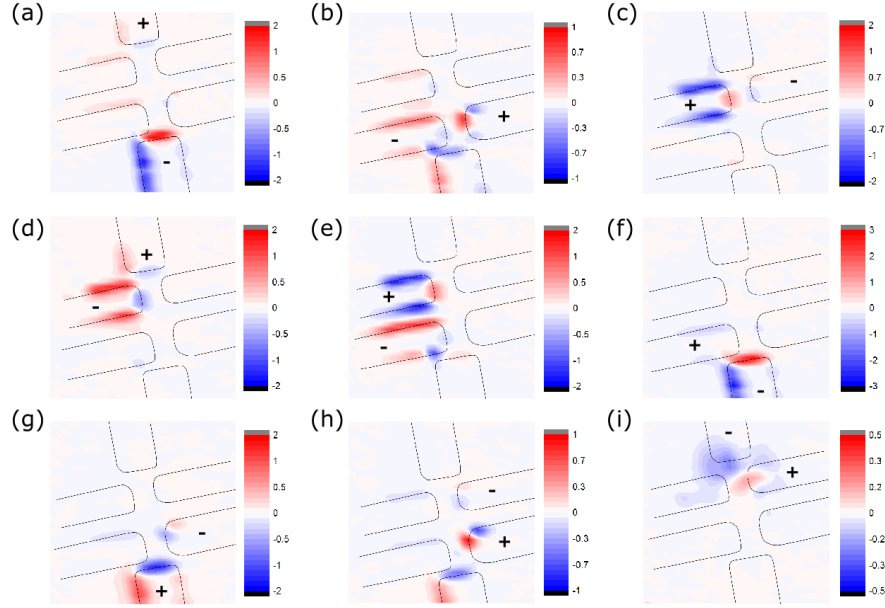


Fig. S4. Circular photocurrent map at low temperature (140K) for various electrode pair configurations. All of these data are obtained using 720 nm optical excitations with optical power between 90 to 100 μ W. The unit of the circular photocurrent is nA. The circular photocurrent map is qualitatively similar to the room temperature case but with much bigger circular photocurrent magnitude. The (+)/(-) indicates the current-collecting electrode, i.e. the current is positive if it flows from the (+) electrode to the (-) electrode. The source-drain bias is not applied.

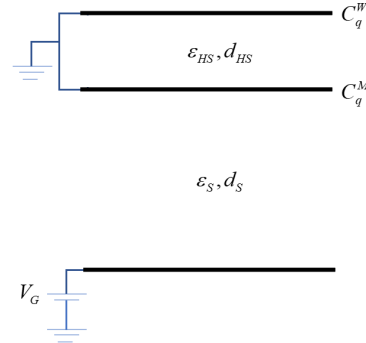


Fig. S5. Equivalent circuit model for the region under the electrode. Here, $C_q^{M(W)}$ is the quantum capacitance of the MoS₂ (WSe₂) layer, $\epsilon_{S(HS)}$ and $d_{S(HS)}$ are the dielectric constant and the thickness of the SiO₂ substrate (MoS₂/WSe₂ heterostructure), respectively, and V_G is the back gate voltage.

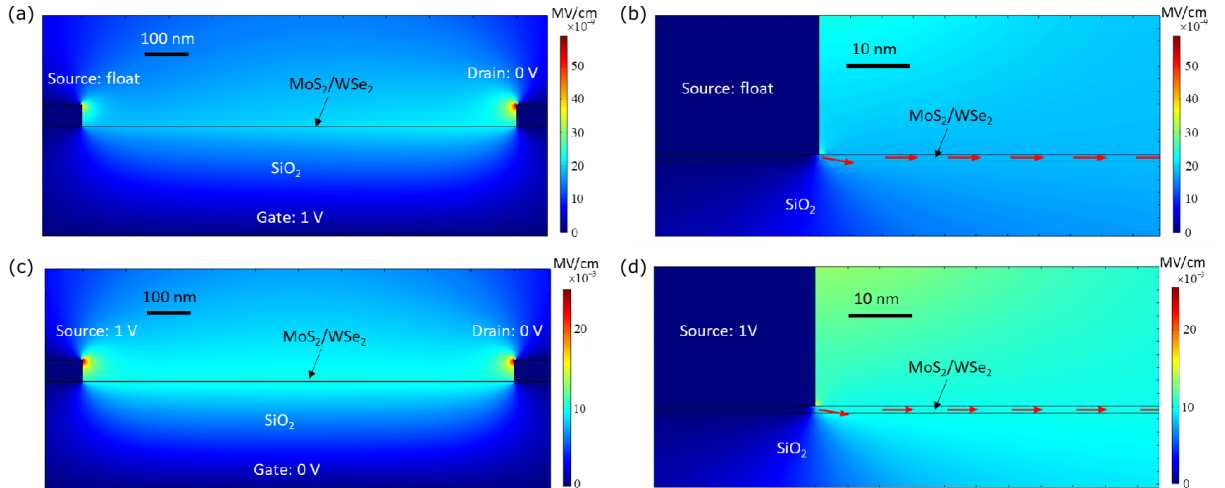


Fig. S6. Simulation of the electric field due to the electric potential caused by the back gating and the source-drain bias. (a, b) The in-plane electric field magnitude due to the back gating. The scale bar is in 10^{-9} MV/cm. The plot in (b) is the zoomed part near the source electrode. The red arrows show the direction of the total electric field in the heterostructure. (c, d) The in-plane electric field magnitude due to the source-drain bias. The scale bar is in 10^{-3} MV/cm. The plot in (d) is the zoomed part near the source electrode. The in-plane electric field due to the source-drain bias is much larger than that due to the back gating.

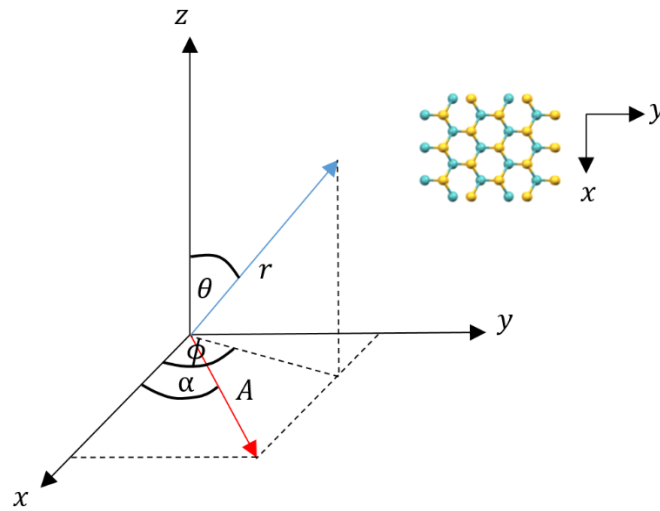


Fig. S7. Space coordinate definition used in the report.

References

1. C. Jiang, W. Xu, A. Rasmita, Z. Huang, K. Li, Q. Xiong, and W.-b. Gao, "Microsecond dark-exciton valley polarization memory in two-dimensional heterostructures," *Nature communications* **9**, 753 (2018).
2. T. Yu and M. Wu, "Valley depolarization due to intervalley and intravalley electron-hole exchange interactions in monolayer MoS₂," *Physical Review B* **89**, 205303 (2014).
3. H. Yu, Y. Wu, G.-B. Liu, X. Xu, and W. Yao, "Nonlinear valley and spin currents from Fermi pocket anisotropy in 2D crystals," *Physical review letters* **113**, 156603 (2014).
4. J. Lee, Z. Wang, H. Xie, K. F. Mak, and J. Shan, "Valley magnetoelectricity in single-layer MoS₂," *Nature materials* **16**, 887 (2017).
5. Y. Meng, T. Wang, C. Jin, Z. Li, S. Miao, Z. Lian, T. Taniguchi, K. Watanabe, F. Song, and S.-F. Shi, "Electrical switching between exciton dissociation to exciton funneling in MoSe₂/WS₂ heterostructure," *Nature Communications* **11**, 2640 (2020).
6. Q. Zhu, M. W.-Y. Tu, Q. Tong, and W. Yao, "Gate tuning from exciton superfluid to quantum anomalous Hall in van der Waals heterobilayer," *Science advances* **5**, eaau6120 (2019).
7. Z. Wang, Y.-H. Chiu, K. Honz, K. F. Mak, and J. Shan, "Electrical tuning of interlayer exciton gases in WSe₂ bilayers," *Nano Letters* **18**, 137-143 (2018).